Nigerian Journal of Physics (NJP)
ISSN online: 3027-0936
ISSN print: 1595-0611
DOI: https://doi.org/10.62292/njp.v35i4.2026.636
Volume 35(4), December 2026

Simulation and Optimization of CdTe and CIGS Thin-Film Solar Cells with Dual ETLS (CdS, ZnO) Using SCAPS-1D: A Comparative Approach

[1]Damian E. Adukwu, *[2]Solomon D. Igba, [3,4,5]Peverga R. Jubu and [1]Adebayo Ademola

[1]Department of Physics, Nigeria Maritime University, Delta State, Nigeria.
[2]Department of Physics, College of Physical Sciences, Joseph Sarwuan Tarkaa University Makurdi, Benue State, Nigeria.
[3]Africa Centre of Excellence in Future Energies and Electrochemical Systems (ACE-FUELS), Federal University of Technology Owerri (FUTO), P.M.B. 1526 Owerri, Imo State, Nigeria.
[4]Institute of Nano-Optoelectronics Research and Technology (INOR), Universiti Sains Malaysia, 11800 USM, Penang, Malaysia.
[5]Department of Industrial Physics, Joseph Sarwuan Tarka University, Makurdi P.M.B. 2373, Makurdi, Benue State, Nigeria.

*Corresponding Author's Email: denensolomon41@gmail.com
ORCID iD: https://orcid.org/0009-0001-0395-3128

Keywords:
CdTe thin-film solar cells, CIGS photovoltaics, SCAPS-1D simulation, Electron transport layers (CdS, ZnO), Absorber thickness optimization.

Submitted: 30 Jun. 2026
Accepted: 20 Jul. 2026
Published: 27 Jul. 2026

ABSTRACT

Thin-film solar cells offer promising alternatives to crystalline silicon photovoltaics, combining reduced material consumption with flexibility and cost-effectiveness. Among them, cadmium telluride (CdTe) and copper indium gallium selenide (CIGS) remain the most commercially successful technologies, though their performance depends strongly on structural and electronic parameters. This work employs SCAPS-1D simulations to investigate CdTe- and CIGS-based devices incorporating two electron transport layers (ETLs), cadmium sulfide (CdS) and zinc oxide (ZnO). The analysis explores absorber and ETL thickness, doping concentration, interface defect density, and bulk defect density. Baseline simulations show that CdTe devices achieved efficiencies of 18.7% (Voc = 0.59 V, Jsc = 43 mA/cm²), while CIGS devices reached up to 35.1% efficiency (Voc = 1.37 V, Jsc = 28 mA/cm²). Correlation studies reveal that CdTe efficiency improvements are mainly linked to doping-driven increases in Voc and FF, whereas CIGS efficiency is governed by Jsc enhancements from optimized thickness. CdTe demonstrated tolerance to interface and defect variations, in contrast to CIGS, which exhibited efficiency collapse under high recombination conditions. The novelty of this study lies in its comparative and integrated optimization of CdTe and CIGS using two ETLs under identical SCAPS-1D conditions, bridging a gap in prior literature where these absorbers are typically studied separately. The findings highlight a trade-off: CIGS provides higher efficiencies but requires strict defect and interface control, while CdTe offers robustness under fabrication variability. These results inform both material selection and device engineering strategies for advancing scalable thin-film photovoltaic technologies.

INTRODUCTION

The global energy transition is accelerating under the dual pressures of climate change and rising electricity demand, with photovoltaics (PV) positioned at the forefront of renewable energy adoption (Mabvuer *et al.*, 2023). Crystalline silicon remains dominant, providing more than 90% of global PV capacity, yet its high material use, rigidity, and cost motivate interest in thin-film alternatives (Lu *et al.*, 2021). Thin-film solar cells, with their lightweight form factor and reduced absorber requirements, offer a pathway to scalable, flexible, and cost-competitive solutions (Tyagi *et al.*, 2013).

Among thin-film technologies, cadmium telluride (CdTe) and copper indium gallium selenide (CIGS) have

emerged as the most commercially successful. CdTe is valued for its nearly ideal bandgap (~1.45 eV) and high absorption coefficient, enabling strong current generation with thinner layers (Kasap, 2006). By contrast, CIGS offers a tunable bandgap (1.0–1.7 eV depending on Ga ratio), superior defect tolerance under optimized growth, and record efficiencies above 23% (Osman *et al.*, 2020; Nakamura *et al.*, 2019; Aungwa *et al*., 2025). These two technologies are thus leading candidates for complementing or even displacing crystalline silicon in the next generation of PV deployment.

Nevertheless, challenges remain. CdTe devices are typically limited by open-circuit voltage (Voc) deficits, preventing them from achieving their theoretical efficiency limits (Mazur *et al.*, 2023). CIGS cells, while capable of excellent performance, are highly sensitive to interface quality and defect densities, which can introduce recombination losses and destabilize performance (Ramanujam & Singh, 2017; Hernández-Gutiérrez *et al.*, 2019). Additionally, the widespread use of cadmium sulfide (CdS) as the conventional electron transport layer (ETL) poses drawbacks due to its ~2.4 eV bandgap and associated parasitic absorption in the blue spectrum, reducing current collection (Hua, 2022). ZnO has been proposed as an alternative ETL because of its higher bandgap and transparency, with promising results in simulation and experiment (Albiss & Al-Widyan, 2023; Saravanan & Rajasekaran, 2022).

Over the last two decades, significant progress has been made in optimizing CdTe and CIGS separately. In CdTe, studies have examined absorber doping (Efaz *et al.*, 2022), back-contact engineering (Eltamaly & Mohamed, 2021), and defect passivation strategies (Saravanan & Rajasekaran, 2022). For CIGS, efforts have focused on bandgap profiling (Ramanujam & Singh, 2017), absorber composition (Jackson *et al.*, 2016), defect density reduction (Green *et al.*, 2020), and interface passivation (Rau & Schock, 2010). Simulation studies using SCAPS-1D and related tools have expanded rapidly, providing predictive insights into parameter tuning (Burgelman *et al.*, 2005; Bencherif *et al.*, 2022; Boughanbour *et al.*, 2025). Recent works extend even beyond CdTe and CIGS to perovskites and tandem devices, where absorber/ETL optimization parallels the thin-film design strategies explored here (Bencherif *et al.*, 2022; Danladi *et al.*, 2025a; Danladi *et al.*, 2025b; Danladi *et al.*, 2025c).

Despite this progress, most investigations treat CdTe and CIGS in isolation, leaving a gap in comparative analyses under unified modeling conditions. Few studies systematically explore how absorber thickness, ETL properties, doping, and defects impact both technologies side by side. Such comparative insights are critical for guiding material choice and processing priorities in industrial deployment.

The novelty of this study lies in addressing this gap. By simulating CdTe and CIGS devices with CdS and ZnO ETLs under identical SCAPS-1D conditions, and by systematically varying absorber and ETL thickness, doping, defect density, and interface quality, this work provides a comprehensive comparative analysis. Unlike prior isolated studies, the present work correlates I–V characteristics, quantum efficiency (QE) spectra, and efficiency trends, generating a holistic picture of how these parameters influence device performance.

The objectives of the study are threefold:

i. to establish baseline device performance for CdTe and CIGS with CdS and ZnO ETLs,
ii. to analyze the influence of absorber thickness, ETL thickness, doping, interface defects, and bulk defect density on Voc, Jsc, FF, and PCE, and
iii. to identify trade-offs between robustness and peak efficiency in CdTe and CIGS cells.

By doing so, this work contributes both to the optimization of individual absorbers and to the comparative understanding of thin-film solar cells, informing strategies for scalable, high-performance photovoltaic deployment.

MATERIALS AND METHODS

This study employed the Solar Cell Capacitance Simulator (SCAPS-1D), developed at the University of Ghent, as the primary modeling tool for device simulations (Burgelman *et al.*, 2005). SCAPS-1D is widely used in thin-film solar cell research because it solves Poisson's equation and continuity equations for electrons and holes across multilayer device structures, thereby enabling predictive analyses of current–voltage (I–V) characteristics, quantum efficiency (QE) spectra, and recombination dynamics under varying device conditions (Bencherif *et al.*, 2022; Boughanbour *et al.*, 2025). Its use has been validated in several CdTe, CIGS, and perovskite studies, where simulation results correlate strongly with experimental findings (Efaz *et al.*, 2022; Bencherif *et al.*, 2022; Danladi *et al.*, 2025a).

Governing Equations for Simulation

SCAPS solves the following fundamental equations to model charge generation, transport, and recombination.

Poisson's Equation

This relates electrostatic potential to space charge density (Danladi *et al.*, 2025a).

$$\frac{d^2\psi(x)}{dx^2} = -\frac{q}{\varepsilon_o \varepsilon_r}\left(p(x) - n(x) + {N_D}^+ - {N_A}^- + \rho_p - \rho_n\right) \quad (1)$$

Where ψ(x) is the electrostatic potential, q is the elementary charge, ε_o and ε_r are the vacuum and relative permittivity, n(x), p(x) are electron and hole concentrations, ${N_D}^+ \; and \; {N_A}^-$ are donor and acceptor densities, $\rho_p \; and \; \rho_n$ are additional charge densities due to interface states or defects.

Continuity Equations

Charge transport is governed by:

Electron current:

$$J_n = qn\mu_n\varepsilon + qD_n\frac{\partial n}{\partial x} \quad (2)$$

Hole Current Density Equation

$$J_p = qp\mu_p\varepsilon - qD_p\frac{\partial p}{\partial x} \quad (3)$$

Where μ_n and μ_p are mobilities, D_n *and* D_p diffusion coefficients, ε electric field (Ramanujam & Singh, 2017; Danladi et al., 2025a; Bencherif *et al.,* 2022).

Shockley–Read–Hall (SRH) Recombination

This governs defect-assisted recombination:

$$R_{SRH} = \frac{n_p - {n_i}^2}{\tau_p(n+n_t)+\tau_n(n+n_t)} \quad (4)$$

Carrier lifetimes depend on:

$$\tau = \frac{1}{\sigma N_t v_{th}} \quad (5)$$

Where σ capture cross-section, N_t defect/trap density, v_{th} thermal velocity Where σ is the capture cross-section, N_t is the defect/trap density, and v_th is the thermal velocity (Danladi *et al.*, 2025a; Bencherif *et al.*, 2022).

Device Structures

Four device architectures were modeled in this work: CdS/CdTe, ZnO/CdTe, CdS/CIGS, and ZnO/CIGS. Each structure consisted of a transparent conducting oxide (TCO), the ETL (CdS or ZnO), the absorber (CdTe or CIGS), a back contact, and the substrate. CdS was modeled with a bandgap of 2.4 eV, while ZnO was modeled with a wider bandgap (3.3 eV), consistent with prior reports on ETL optimization (Hua, 2022; Albiss & Al-Widyan, 2023; Benami *et al.*, 2022). CdTe and CIGS absorbers were parameterized according to standard literature values, with bandgaps of 1.45 eV and 1.15 eV, respectively (Kasap, 2006; Osman *et al.*, 2020; Jackson *et al.*, 2016).

Simulation Parameters

Baseline material and device parameters, including layer thicknesses, bandgaps, electron affinities, dielectric constants, doping concentrations, and defect densities, were selected based on literature benchmarks. The use of different input simulation values for the two technologies reflects the distinct material properties and established parameter sets reported in prior experimental and simulation studies for CdTe (Efaz *et al.*, 2022; Eltamaly & Mohamed, 2021) and CIGS (Jackson *et al.*, 2016; Green *et al.*, 2020; Rau & Schock, 2010). These parameter choices ensure that the simulations accurately represent the physical behavior of each material system while enabling a meaningful comparative analysis.

Table 1: Input simulation parameters for the thin film solar cells

Parameters	**Layer**				
	FTO (Bencherif *et al.*, 2022; Danladi *et al.*, 2025a)	**CdS (Hua, 2022; Albiss & Al-Widyan, 2023)**	**ZnO (Danladi *et al.*, 2025a; Benami *et al.*, 2022)**	**CdTe (Mazur *et al.*, 2023)**	**CIGS (Osman *et al.*, 2020; Mabvuer *et al.*, 2023)**
Thickness (μm)	0.4	0.05	0.05	2.00	1.00
Band gap, Eg (eV)	3.5	2.4	3.3	1.10	1.45
Dielectric permittivity, ε_r	4.3	4.5	9.0	4.50	4.40
Electron affinity, χ (eV)	9.0	10.0	4.10	13.60	9.20
CB effective density of states, N_C (cm^{-3})	2.2×10^{18}	2.2×10^{18}	4.0×10^{18}	2.2×10^{18}	1.0×10^{15}
VB effective density of states, N_V (cm^{-3})	1.8×10^{19}	1.8×10^{19}	1.8×10^{19}	1.8×10^{19}	1.0×10^{15}
Electron thermal velocity (cm/s)	1×10^{7}	1×10^{7}	1×10^{7}	1×10^{7}	1×10^{7}
Hole thermal velocity (cm/s)	1×10^{7}	1×10^{7}	1×10^{7}	1×10^{7}	1×10^{7}
Acceptor concentration, N_A (cm^{-3})	0	1×10^{16}	0	1×10^{15}	1×10^{14}
Donor concentration, N_D (cm^{-3})	1×10^{18}	1×10^{16}	1×10^{18}	1×10^{15}	1.0×10^{17}

Electron mobility, μ_n ($cm^2V^{-1}s^{-1}$)	20	100	100	100	320.00
Hole mobility, μ_p ($cm^2V^{-1}s^{-1}$)	10	50	25	25	40.00
Defect density, N_t (cm^{-3})	1×10^{14}	1×10^{14}	1×10^{14}	1×10^{15}	1.0×10^{15}

Table 2: Interface parameters for the solar cells (Danladi *et al.*, 2025a)

Parameters	CdS/CdTe interface	ZnO/CIGS interface
Defect type	Neutral	Neutral
Cross section for electrons (cm^2)	1×10^{-19}	1×10^{-19}
Cross section for holes (cm^2)	1×10^{-19}	1×10^{-19}
Energetic distribution	Single	Single
Energy level with respect to EV (eV)	0.65	0.65
Characteristic energy (eV)	0.10	0.10
Total density (cm^{-2})	1×10^{10}	1×10^{10}

The operating temperature was set at 300 K, with standard AM1.5G illumination conditions (1000 W/m²)

Output Metrics

The simulation outputs included:

Current–voltage (I–V) characteristics, from which open-circuit voltage (Voc), short-circuit current density (Jsc), fill factor (FF), and power conversion efficiency (PCE) were extracted.

Quantum efficiency (QE) spectra, indicating wavelength-dependent carrier collection.

Correlation plots between efficiency and electrical parameters to identify key performance drivers.

These outputs were analyzed to assess how thickness, doping, interface quality, and defect density influence device behavior. To ensure relevance, simulation trends were compared with recent literature on CdTe, CIGS, and related thin-film or perovskite devices (Nakamura *et al.*, 2019; Eltamaly & Mohamed, 2021; Bencherif *et al.*, 2022; Danladi *et al.*, 2025c).

RESULTS AND DISCUSSION

Baseline Device Performance

The baseline metrics of the four simulated devices are summarized in Table 3, revealing clear contrasts between CdTe- and CIGS-based architectures. The CdS/CdTe configuration achieved a Voc of 0.59 V, Jsc of 43.31 mA/cm², FF of 73.32%, and PCE of 18.70%. Replacing CdS with ZnO as the ETL slightly reduced efficiency to 17.82%, driven by a small decline in FF. In comparison, the CdS/CIGS device reached a much higher PCE of 33.29% (Voc = 1.37 V, Jsc = 27.05 mA/cm², FF = 89.93%). The ZnO/CIGS device outperformed all others, achieving 35.08% efficiency with Voc of 1.37 V, Jsc of 28.42 mA/cm², and FF of 90.11%.

Table 3: Prototype solar cell parameters deduced from calculated IV-curve

Solar Cell	Voc (V)	Jsc (mA/cm²)	FF (%)	PCE (%)
CdS/CdTe	0.59	43.31	73.32	18.70
ZnO/CdTe	0.590882	43.28207900	69.6821	17.8209
CdS/CIGS	1.368527	27.05265365	89.9271	33.2931
ZnO/CIGS	1.370	28.42	90.11	35.08

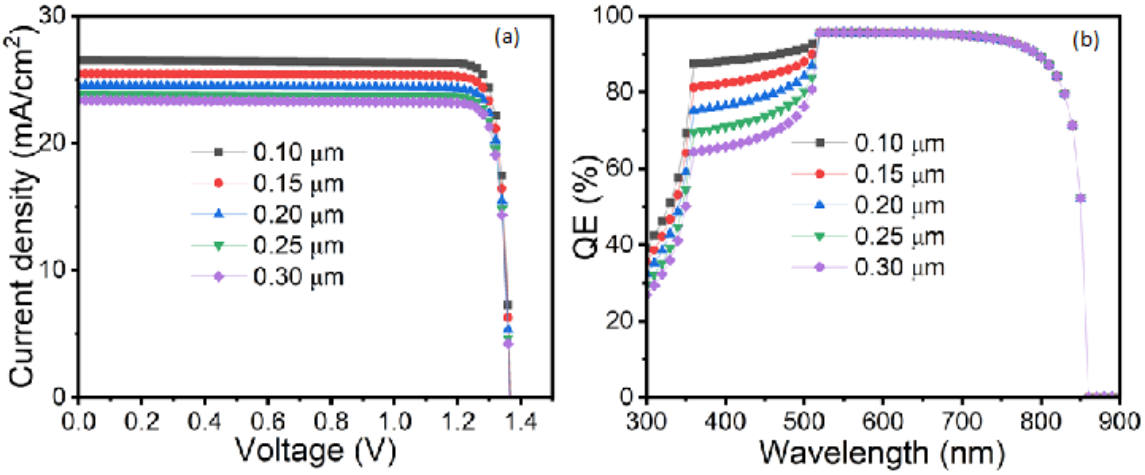

Figure 1: (a) J-V curves with various CdS ETL thicknesses, (b) QE plots with various CdS ETL layer thicknesses under illumination

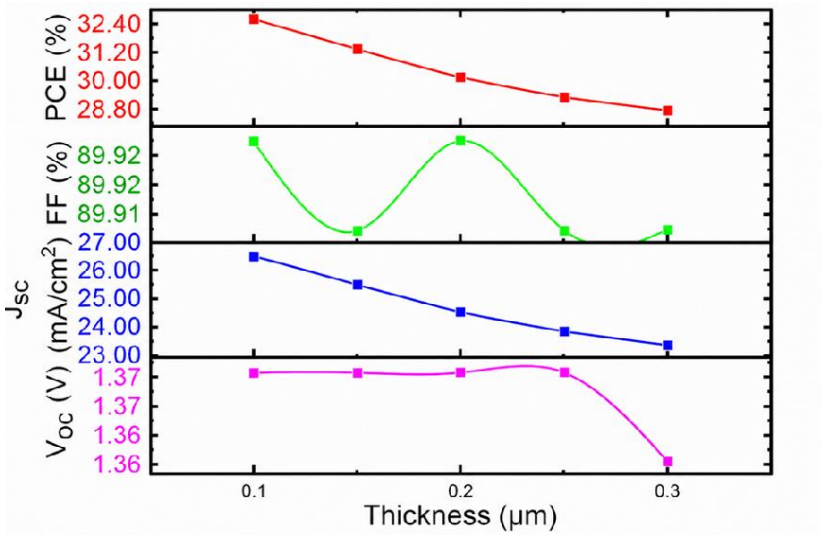

Figure 2: Correlation between V_{OC}, J_{SC}, FF and PCE with CdS ETL thicknesses

These differences are visually evident in the I–V curves (Figure 1a for CdTe; Figure 7a for CIGS). CdTe-based devices generate higher photocurrent densities but show weaker rectification, reflected in their lower FF values. CIGS devices, by contrast, exhibit steeper slopes and nearly ideal diode behavior, explaining their superior FF and overall performance.

The QE spectra (Figure 1b for CdTe; Figure 7b for CIGS) complement this observation. CdTe cells show strong absorption between 400–800 nm, consistent with their 1.45 eV bandgap, but their response diminishes sharply at longer wavelengths. CIGS cells, however, extend spectral response into the near-infrared due to their narrower bandgap (1.15 eV), enhancing photocurrent generation.

Correlation graphs provide further insight. As shown in Figure 2 (CdTe), efficiency trends are strongly coupled to Jsc variations, while Figure 8 (CIGS) indicates that Voc and FF are the dominant performance drivers. These findings align with experimental literature: CdTe's efficiency is often limited by Voc deficits (Mazur *et al.*, 2023), whereas CIGS excels in FF and Voc under optimized processing (Nakamura *et al.*, 2019; Osman *et al.*, 2020).

The overall baseline results confirm earlier reports that ZnO, owing to its wider bandgap and reduced parasitic absorption, improves Jsc relative to CdS (Hua, 2022; Albiss & Al-Widyan, 2023). At the same time, the data emphasize the inherent trade-off: CdTe is a robust current-generating material but struggles with voltage, while CIGS offers superior voltage and fill factor at the expense of stronger sensitivity to defects (Ramanujam & Singh, 2017; Hernández-Gutiérrez *et al.*, 2019).

Effect of ETL Thickness

ETL thickness variations had subtle but observable effects on device performance.

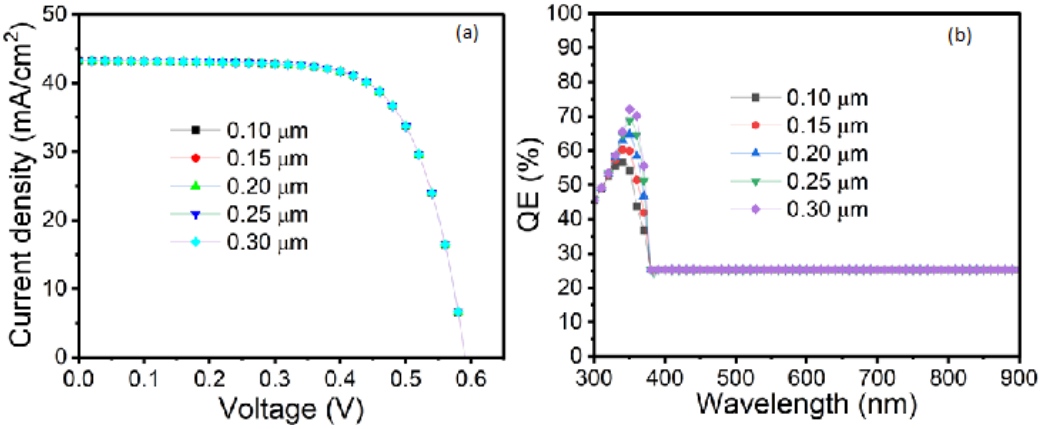

Figure 3: (a) J-V curves with various ZnO ETL thicknesses, (b) QE plots with various ZnO ETL layer thicknesses under illumination

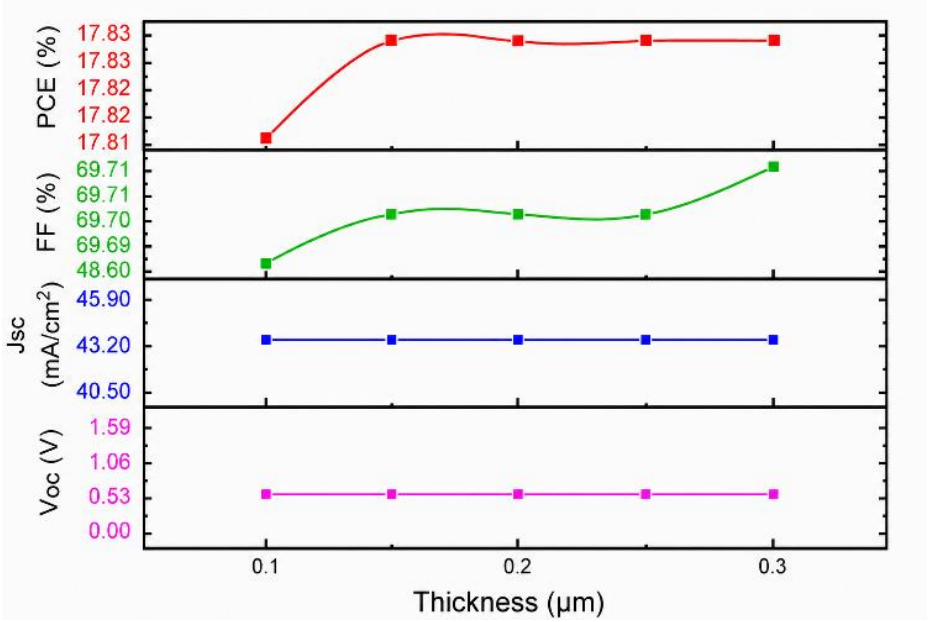

Figure 4: Correlation between V_{OC}, J_{SC}, FF and PCE with ZnO ETL thicknesses

Figures 3a and 4a show the I–V curves for CdS and ZnO ETL thickness variations, respectively. Increasing CdS or ZnO thickness reduced Jsc slightly, with corresponding QE suppression at short wavelengths (Figures 3b and 4b). The correlation graphs (Figures 2 and 6) confirm modest efficiency declines, consistent with Hua (2022) and Albiss & Al-Widyan (2023), who recommend minimal ETL thickness to reduce parasitic absorption.

For CdTe devices, the CdS ETL thickness variation from 0.01 to 0.30 µm resulted in efficiency changes primarily driven by Jsc variations, as shown in Figure 2. The ZnO ETL thickness variation similarly affected device performance, with Figure 4 demonstrating that efficiency trends correlate strongly with Jsc. These results align with Benami *et al.* (2022), who reported that ZnO, with its wider bandgap, provides better blue response compared to CdS.

Effect of Absorber Thickness

The thickness of absorber layers exerted contrasting influences on CdTe and CIGS devices.

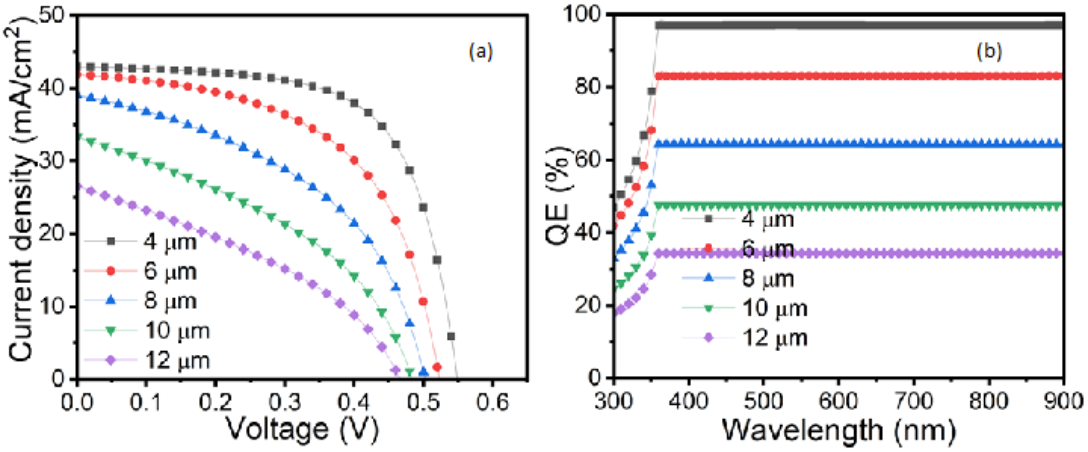

Figure 5: (a) J-V curves with various CdTe absorber layer thicknesses, (b) QE plots with various CdTe absorber layer thicknesses under illumination

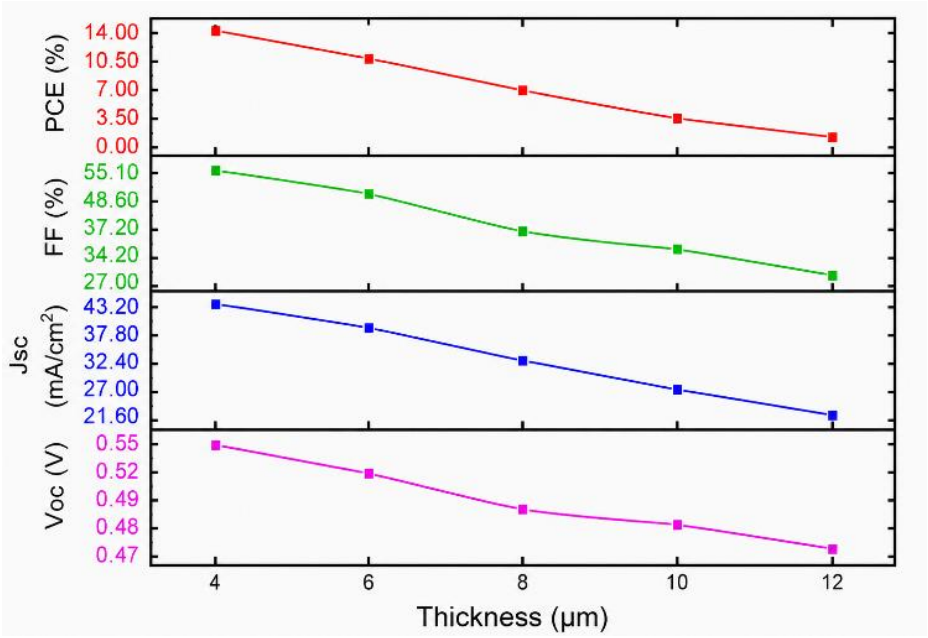

Figure 6: Correlation between V_{OC}, J_{SC}, FF and PCE with CdTe absorber thicknesses

In CdTe, increasing thickness from 4 µm to 12 µm led to reduced performance. As seen in the I–V curves (Figure 5a), thicker CdTe layers displayed weaker rectification, while the QE spectra (Figure 5b) revealed declining carrier collection at longer wavelengths. This effect is quantified in the correlation plot (Figure 6), where efficiency decreased from 15.38% at 4 µm to 4.55% at 12 µm, largely due to a fall in Voc (0.55 → 0.47 V) and Jsc (42.94 → 26.53 mA/cm²). This finding is consistent with Singh and Kushwaha (cited in Mazur *et al.*, 2023), who observed that excessive CdTe thickness increases bulk recombination, outweighing absorption benefits.

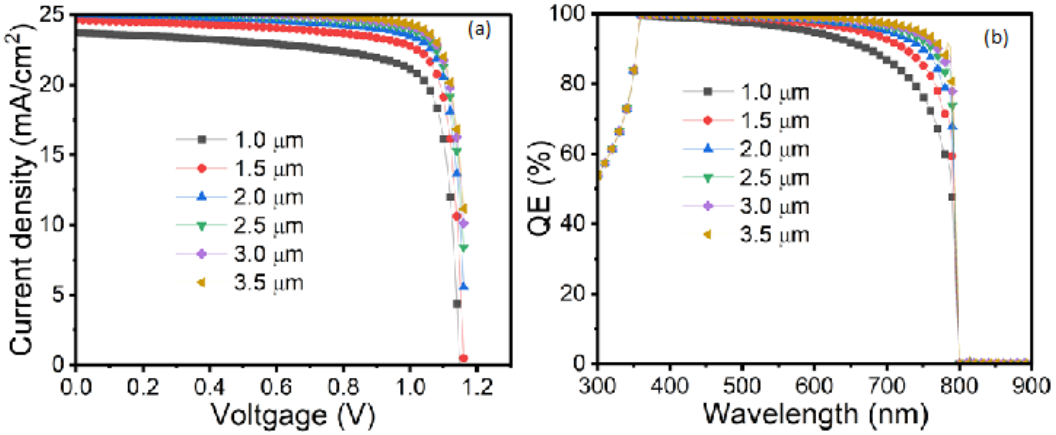

Figure 7: (a) J-V curves with various CIGS absorber layer thicknesses, (b) QE plots with various CIGS absorber layer thicknesses under illumination

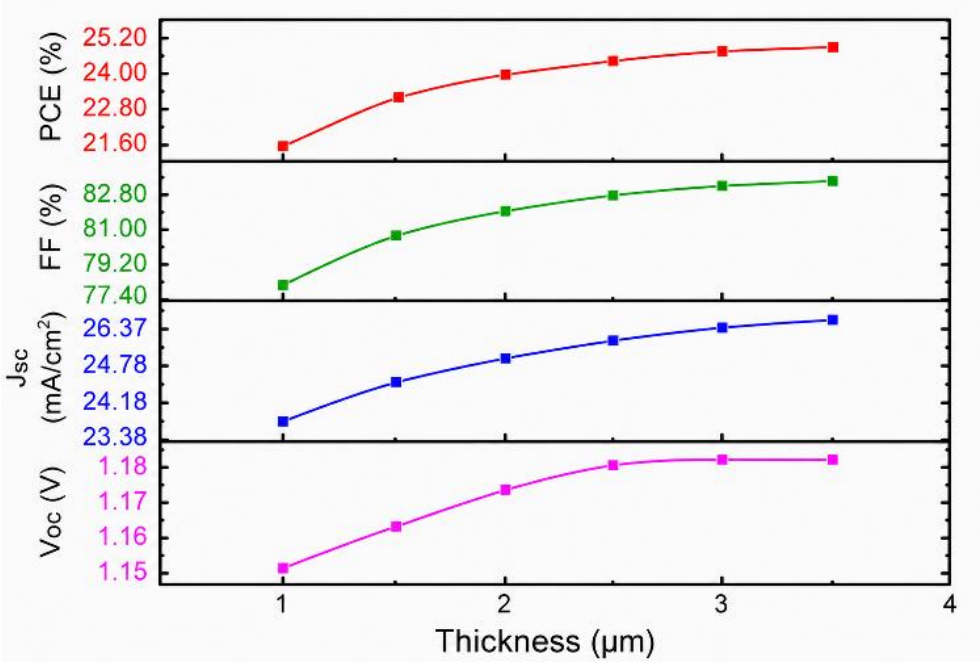

Figure 8: Correlation between V_{OC}, J_{SC}, FF and PCE with CIGS absorber thicknesses

CIGS absorbers behaved differently. As thickness increased from 1 µm to 3.5 µm, the I–V curves (Figure 7a) demonstrated rising photocurrent, while the QE spectra (Figure 7b) showed stronger near-infrared response. The correlation graph (Figure 8) confirms efficiency growth from 21.23% to 25.03%, driven mainly by Jsc gains (23.70 → 25.49 mA/cm²), while Voc improved slightly (1.15 → 1.18 V). This aligns with Jackson *et al.* (2016) and Nakamura *et al.* (2019), who stressed that sufficient CIGS thickness is necessary to harvest long-wavelength photons.

Effect of ETL Doping Concentration

ETL doping adjustments (1×10^{17} to 1×10^{20} cm^{-3}) had modest impact on device performance.

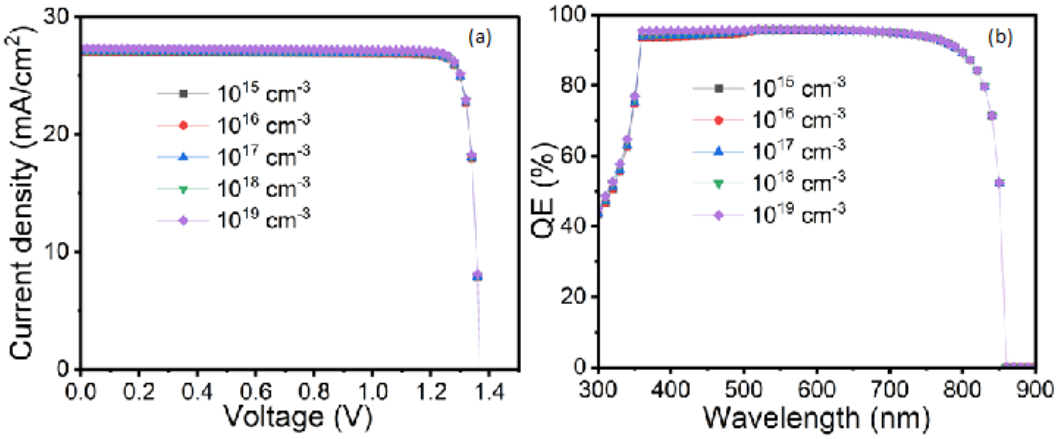

Figure 9: (a) J-V curves with various CdS ETL layer doping concentrations, (b) QE plots with various CdS ETL layer doping concentrations under illumination

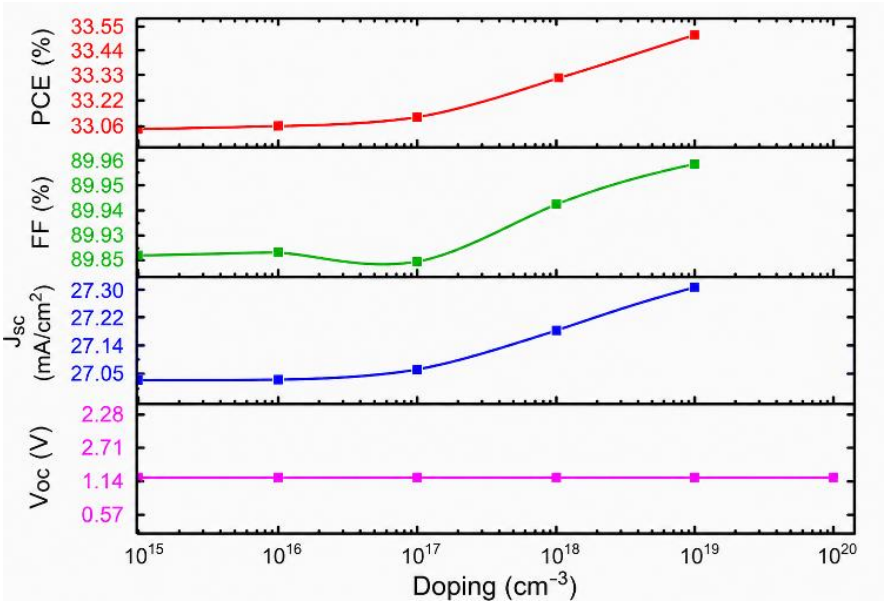

Figure 10: Correlation between V_{OC}, J_{SC}, FF and PCE with CdS ETL layer doping concentrations

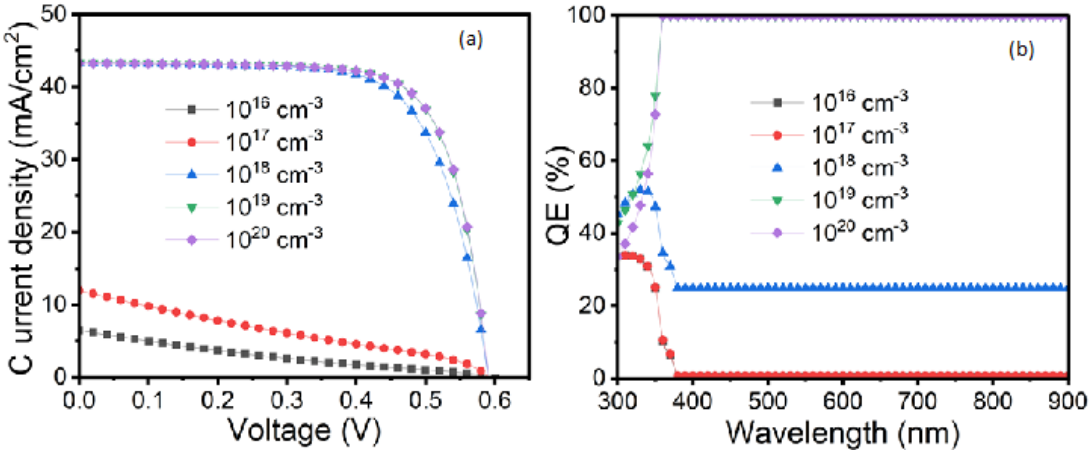

Figure 11: (a) J-V curves with various ZnO ETL layer doping concentrations, (b) QE plots with various ZnO ETL layer doping concentrations under illumination

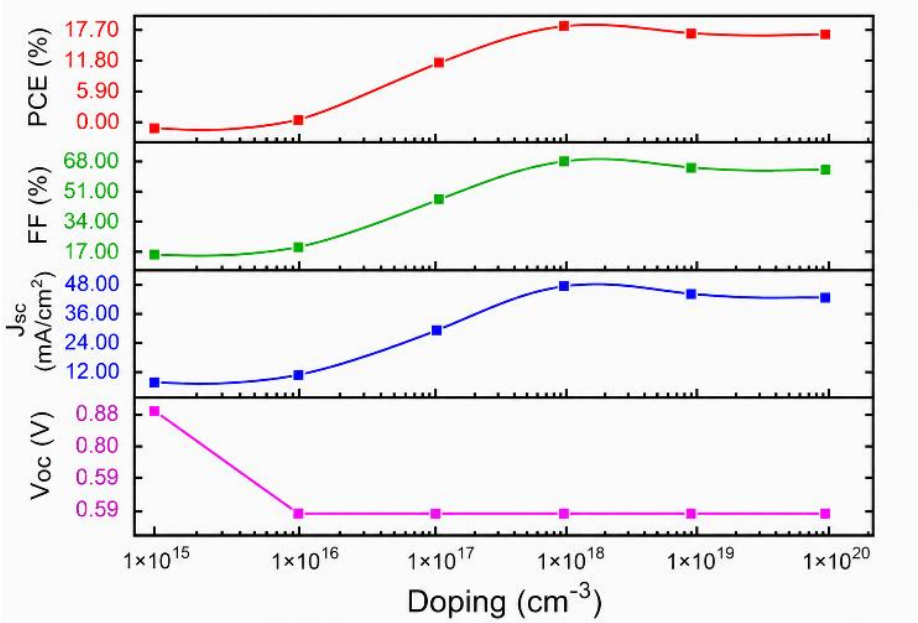

Figure 12: Correlation between V_{OC}, J_{SC}, FF and PCE with ZnO ETL layer doping concentrations

The I–V curves (Figures 9a and 11a for CdS and ZnO, respectively) show slightly improved slopes, but the QE spectra (Figures 9b and 11b) remain almost unchanged. Correlation graphs (Figures 10 and 12) confirm limited efficiency effects, supporting Mabvuer *et al.* (2023), who highlighted absorber doping as the critical optimization factor.

Effect of Absorber Doping Concentration

Doping concentration strongly influenced both absorbers, though with different trends.

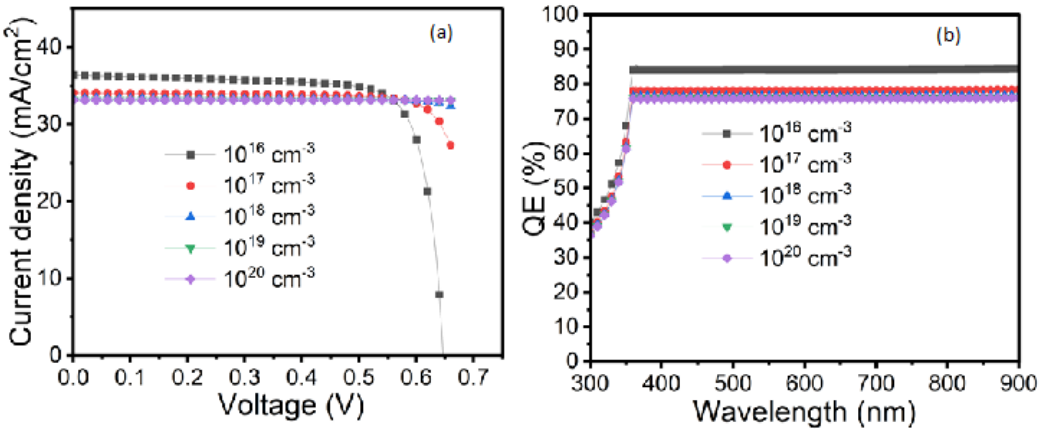

Figure 13: (a) J-V curves with various CdTe absorber layer doping concentrations, (b) QE plots with various CdTe absorber layer doping concentrations under illumination

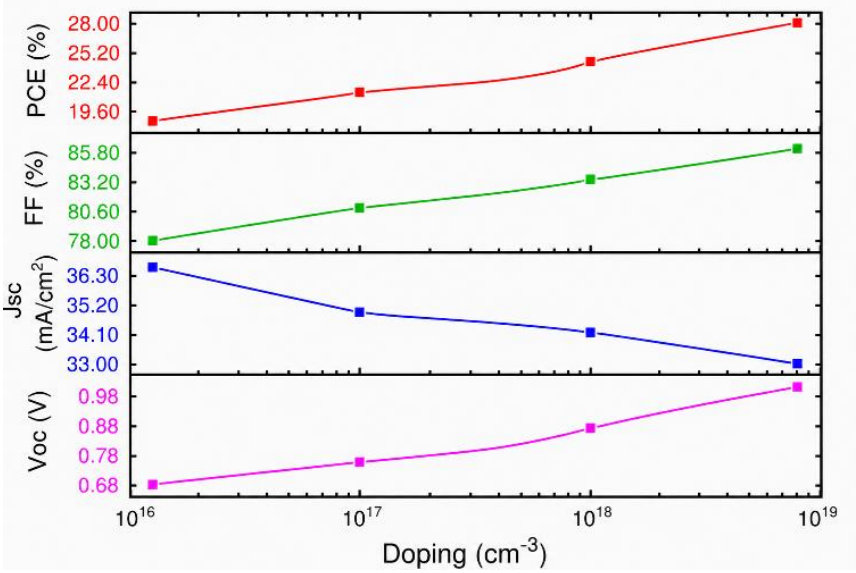

Figure 14: Correlation between V_{OC}, J_{SC}, FF and PCE with CdTe absorber layer doping concentrations

In CdTe, increasing doping from 1×10^{16} to 1×10^{19} cm^{-3} significantly improved Voc and FF. The I–V curves (Figure 13a) show steeper slopes at higher doping, while the QE spectra (Figure 13b) exhibit slight improvements in carrier collection. The correlation plot (Figure 14) indicates efficiency rising from 18.52% to 27.16%, driven by Voc (0.65 → 0.95 V) and FF (78.75% → 86.57%). This agrees with Bonnet's findings (cited in Efaz *et al.*, 2022) that stronger built-in fields in CdTe improve charge extraction.

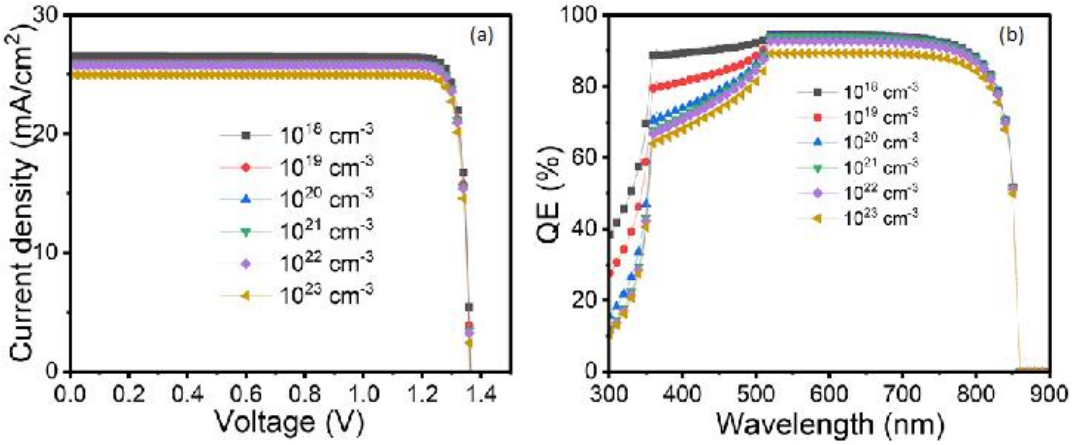

Figure 15: (a) J-V curves with various CIGS absorber layer doping concentrations, (b) QE plots with various CIGS absorber layer doping concentrations under illumination

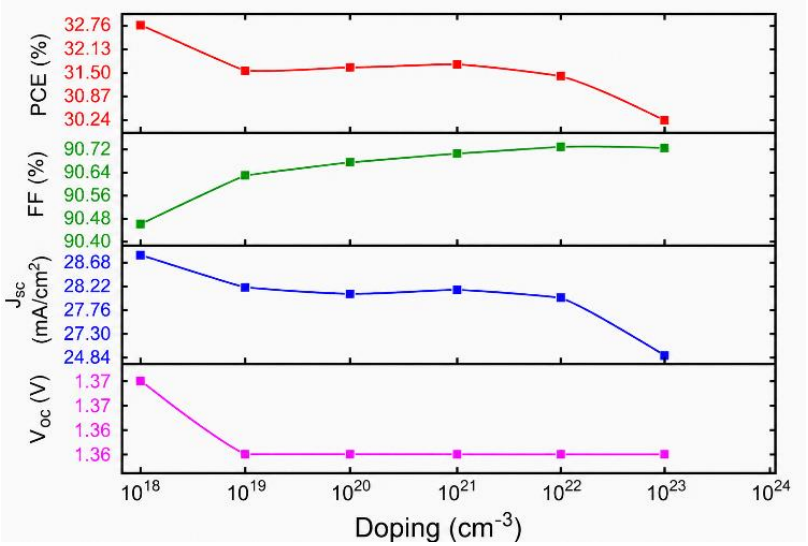

Figure 16: Correlation between V_{OC}, J_{SC}, FF and PCE with CIGS absorber layer doping concentrations

CIGS, however, displayed an optimum. At 1×10^{18} cm^{-3} doping, efficiency peaked at 32.79% (Voc = 1.37 V, Jsc = 26.54 mA/cm², FF = 90.48%). The I–V curve (Figure 15a) at this point shows nearly ideal diode behavior. At higher doping (1×10^{20} cm^{-3}), recombination losses reduced Jsc, visible in the QE spectrum (Figure 15b). The correlation plot (Figure 16) confirms efficiency decline (~31%) at excessive doping. These results mirror Siebentritt and Schmid (cited in Ramanujam & Singh, 2017), who noted reduced carrier lifetimes under over-doping in CIGS.

Effect of Interface Quality

The role of interface defect density diverged significantly between CdTe and CIGS.

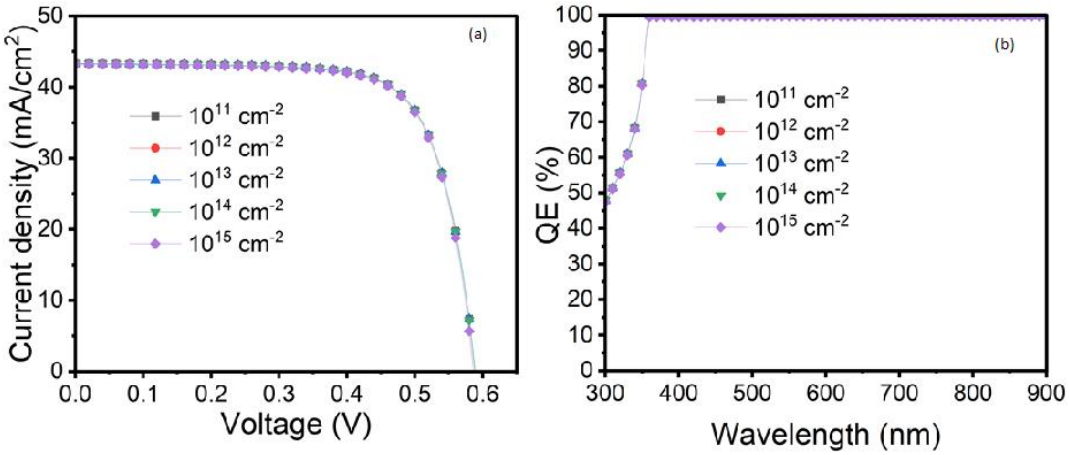

Figure 17: (a) J-V curves with various interface defect densities of CdS/CdTe, (b) QE plots with various interface defect densities of CdS/CdTe under illumination

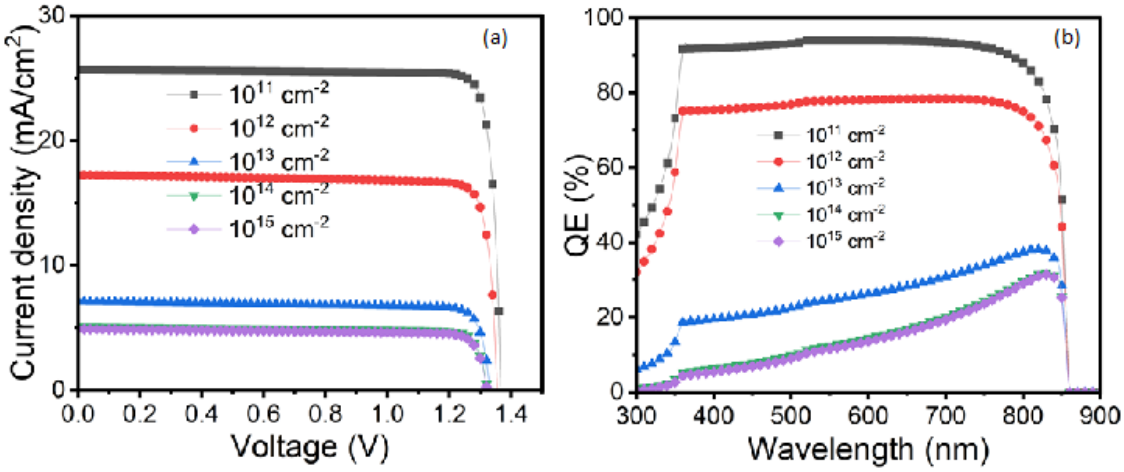

Figure 18: (a) J-V curves with various interface defect densities of CdS/CIGS, (b) QE plots with various interface defect densities of CdS/CIGS under illumination

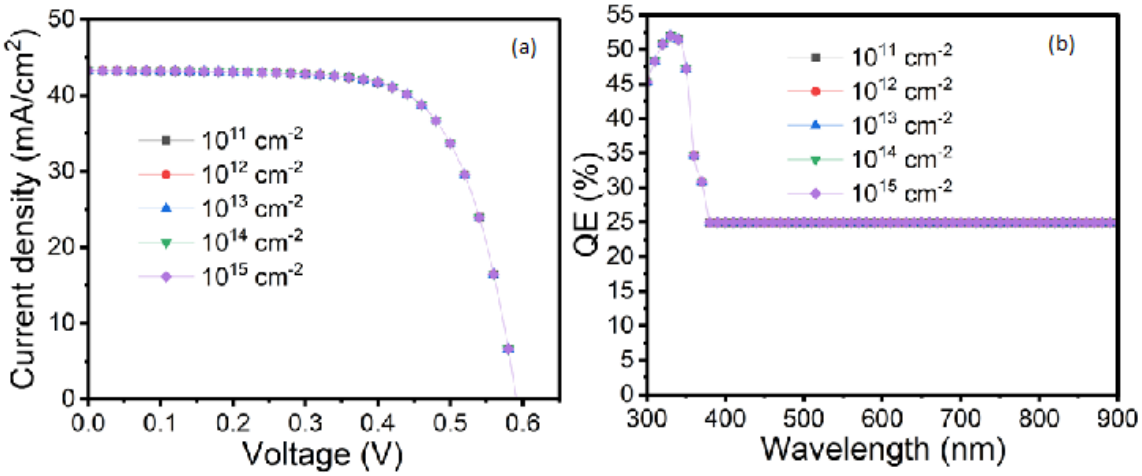

Figure 19: (a) J-V curves with various interface defect densities of ZnO/CdTe, (b) QE plots with various interface defect densities of ZnO/CdTe under illumination

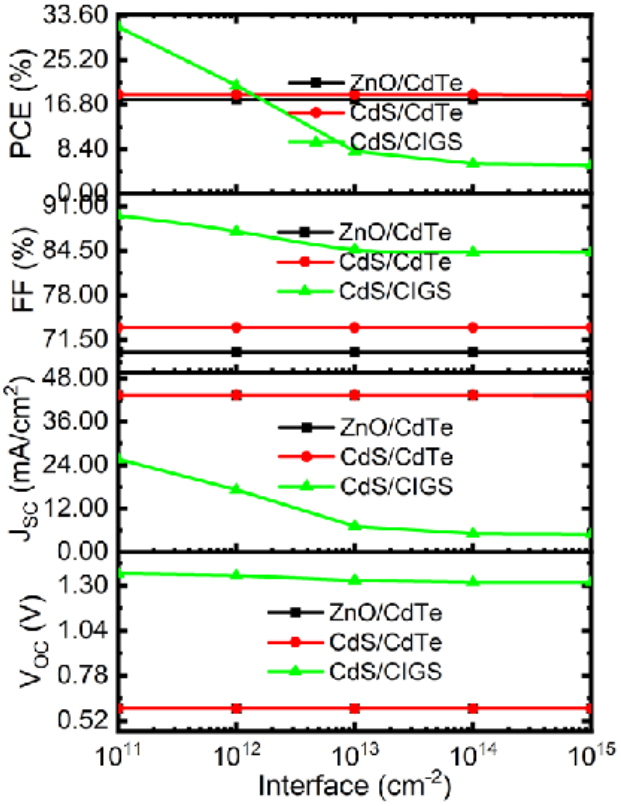

Figure 20: Correlation between V_{OC}, J_{SC}, FF and PCE with interface defect densities of ZnO/CdTe, CdS/CdTe and CdS/CIGS

In CdTe, increasing interface defect density from 1×10^{11} to 1×10^{15} cm^{-2} caused negligible changes. The I–V curves (Figure 17a for CdS/CdTe, Figure 19a for ZnO/CdTe) and QE spectra (Figure 17b, 19b) are nearly identical, while the correlation plot (Figure 20) shows efficiency stable near 18%. This confirms CdTe's resilience, consistent with Saravanan and Rajasekaran (2022).

CIGS showed acute sensitivity. At 1×10^{11} cm^{-2}, the CdS/CIGS device recorded Voc = 1.37 V, Jsc = 25.66 mA/cm², and efficiency of 31.44%. At 1×10^{15} cm^{-2}, the I–V curve (Figure 18a) shows severe current suppression, and the QE spectrum (Figure 18b) demonstrates broad spectral losses. The correlation plot (Figure 20) shows efficiency collapsing to 5.45%, driven by Jsc decline (25.66 → 4.90 mA/cm²). This supports Rau and Schock (2010), who highlighted interface passivation as crucial in CIGS optimization.

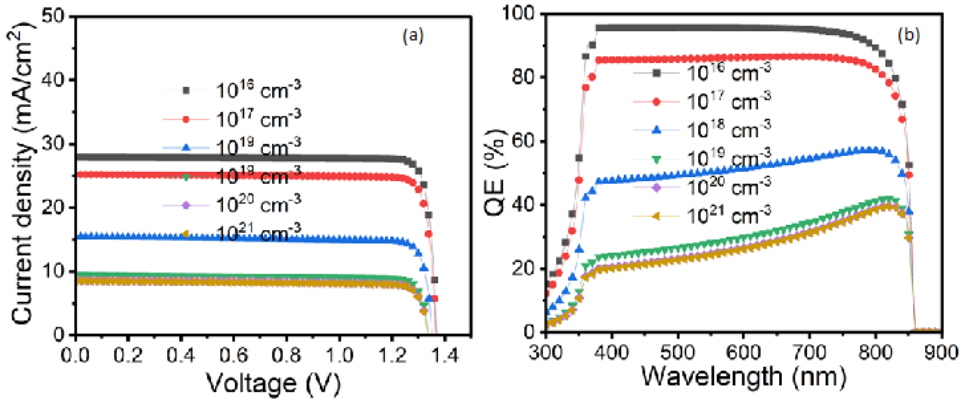

Figure 21: (a) J-V curves with various interface defect densities of ZnO/CIGS, (b) QE plots with various interface defect densities of ZnO/CIGS under illumination

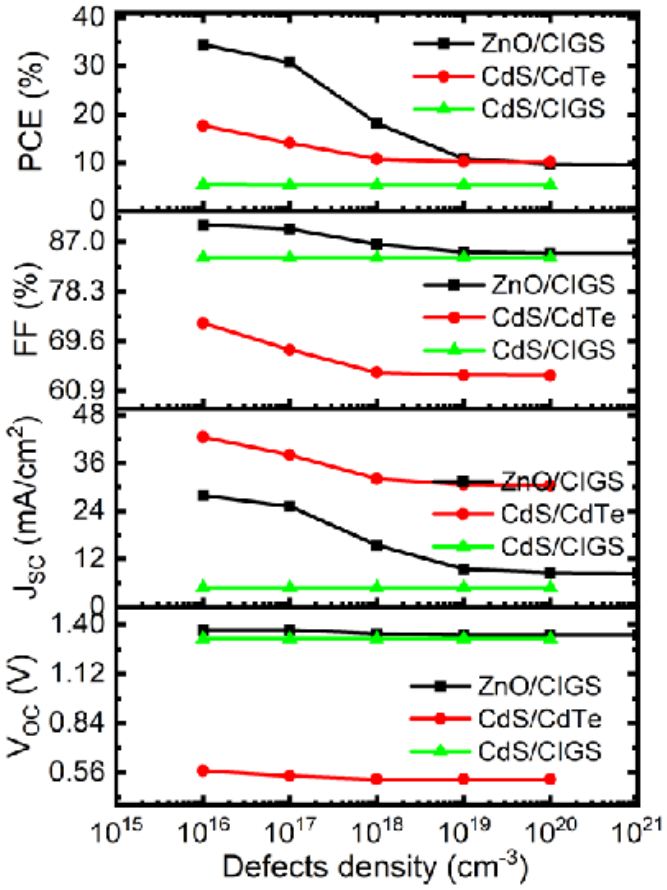

Figure 22: Correlation between V_{OC}, J_{SC}, FF and PCE with interface defect densities of ZnO/CIGS

The ZnO/CIGS interface (Figures 21 and 22) showed similar sensitivity, with efficiency collapsing from ~35% to below 10% as interface defect density increased from 1×10^{11} to 1×10^{15} cm^{-2}. This underscores the critical importance of interface engineering for CIGS-based devices.

In CdTe, increasing defect density from 1×10^{15} to 1×10^{19} cm^{-3} caused modest decreases in Voc (0.57 → 0.52 V) and Jsc (42.48 → 30.51 mA/cm²). The I–V curve (Figure 23a) and QE spectrum (Figure 23b) show slight reductions, but the correlation plot (Figure 26) indicates efficiency remained steady (17–18%) due to FF compensation. This resilience supports Moutinho *et al.* (cited in Mazur *et al.*, 2023), who reported CdTe's high defect tolerance.

CIGS cells, however, degraded sharply with increasing defects. At 1×10^{16} cm^{-3}, efficiency was 34.43% (Jsc = 27.93 mA/cm²), but at 1×10^{21} cm^{-3}, efficiency dropped below 10%. The I–V curve (Figure 24a for CdS/CIGS, Figure 25a for ZnO/CIGS) shows steep current reduction, while the QE spectra (Figures 24b and 25b) highlight severe long-wavelength losses. The correlation graph (Figure 26) confirms strong coupling of efficiency to Jsc. This corroborates Ramanujam and Singh (2017), who emphasized recombination at bulk defects as a major CIGS limitation.

Comparative Analysis

The combined results highlight complementary strengths and weaknesses of CdTe and CIGS. CdTe generates higher photocurrent densities but suffers Voc deficits, limiting peak efficiency. Its robustness to defect and interface variations makes it attractive for scalable manufacturing with less stringent process control. Conversely, CIGS achieves higher efficiencies (>35% with ZnO ETL) through superior Voc and FF, but requires precise optimization of thickness, doping, and defect passivation.

The I–V, QE, and correlation graphs consistently show that CdTe efficiency depends on Voc and FF improvements, particularly with absorber doping, while CIGS performance is dictated by Jsc gains at optimized thickness but collapses under high defect or poor interface conditions. These findings align with Green *et al.* (2020) and Jackson *et al.* (2016), reinforcing CdTe's role as a defect-tolerant industrial material and CIGS's

potential for record efficiencies under controlled fabrication.

Furthermore, comparisons with perovskite simulation studies (Bencherif *et al.*, 2022; Danladi *et al.*, 2025a; Danladi *et al.*, 2025b; Danladi *et al.*, 2025c) underline a broader theme: absorber doping, ETL selection, and defect management are universal levers for improving thin-film photovoltaics. The novelty here lies in the side-by-side CdTe–CIGS analysis with dual ETLs under identical SCAPS-1D conditions, providing a unified framework for optimization that had been missing from prior literature.

CONCLUSION

This study employed SCAPS-1D simulations to systematically compare CdTe and CIGS thin-film solar cells using CdS and ZnO as electron transport layers. The results highlight distinct behaviors: CdTe demonstrated strong photocurrent generation and resilience against interface and bulk defects but remained limited by Voc and FF. CIGS, in contrast, achieved much higher efficiencies (>35%) through superior Voc and FF, particularly with ZnO ETLs, yet was highly sensitive to defect density and interface recombination. These findings emphasize the trade-off between CdTe's robustness and CIGS's efficiency potential, underscoring the importance of context-specific material selection in thin-film PV deployment.

RECOMMENDATIONS

Optimization should prioritize absorber doping to enhance Voc and FF, while maintaining thickness near 4 µm to avoid recombination losses. Its defect tolerance makes CdTe highly suitable for large-scale, lower-cost fabrication environments.

Future research should focus on absorber optimization around 3 µm thickness and doping near 1×10^{18} cm^{-3}, while implementing strict defect and interface passivation strategies. ZnO is the preferred ETL for maximizing efficiency and reducing parasitic absorption losses.

REFERENCES

Albiss, B., & Al-Widyan, M. (2023). Numerical simulation, preparation, and evaluation of Cu(In,Ga)Se_2 (CIGS) thin-film solar cells. ChemEngineering, 7(5), 87. https://doi.org/10.3390/chemengineering7050087

Aungwa, F., Abubakar, A. B., Newton, G. F., Bichi, J. A., Igba, S. D., Adebayo, A. T., Myom, A. M., & Ikyumbur, T. J. (2025). Simulation-based analysis of the breakdown strength of different dielectric materials: A comparative study of polymers, ceramics and composites. Nigerian Journal of Physics, 34(1), 1-12. https://doi.org/10.62292/njp.v34i1.2025.365

Benami, A., Ouslimane, T., Et-taya, L., & Sohani, A. (2022). Comparison of the effects of ZnO and TiO_2 on the performance of perovskite solar cells via SCAPS-1D software package. Journal of Nano-Electronics and Physics, 14, 1–9.

Bencherif, H., Baazouzi, A., Touati, F., & Aida, M. S. (2022). Modeling of high-efficiency planar perovskite solar cell using $(FAPbI_3)_{0.85}(MAPbBr_3)_{0.15}$ as absorber: Simulation and optimization using SCAPS-1D. Materials Today: Proceedings. https://doi.org/10.1016/j.matpr.2022.04.261

Bencherif, H., Meddour, F., Elshorbagy, M. H., Hossain, M. K., et al. (2022). Performance enhancement of $(FAPbI_3)_{1-x}(MAPbBr_3)_x$ perovskite solar cell with an optimized design. Superlattices and Microstructures, 171, 207403. https://doi.org/10.1016/j.spmi.2022.207403

Boughanbour, K., et al. (2025). Simulation and optimization of $MAPbI_3$/$MASnI_3$ heterojunction solar cell perovskite with double ETL by SCAPS-1D software. Optical and Quantum Electronics, 57, 81. https://doi.org/10.1007/s11082-025-08138-8

Burgelman, M., et al. (2005). SCAPS-1D: A solar cell capacitance simulator. Solar Energy Materials and Solar Cells, 85(1), 125–133.

Danladi, E., Jubu, P. R., Tighezza, A. M., Hossain, I., et al. (2025a). Highly efficient, hole transport layer (HTL)-free perovskite solar cell based on lithium-doped electron transport layer by device simulation. Emergent Materials, 6, 1779–1795. https://doi.org/10.1007/s42247-023-00558-0

Danladi, E., Obagboye, L. F., Aisida, S., Ezema, F. I., et al. (2025b). 20.73% highly efficient lead-free $CsSnI_3$-based perovskite solar cells with various charge transport materials: A SCAPS-1D study. Multiscale and Multidisciplinary Modeling, Experiments and Design, 8, 114, 1–21.

Danladi, E., Oguzie, E. E., & Ezema, F. I. (2025c). Highly efficient 25.56% $Cs_2AgBiBr_6$ double perovskite solar cell with copper barium tin sulfide and ZnO as charge transport channels: A theoretical study using SCAPS-1D. Journal of Photonics for Energy, 15(2), 1–38. https://doi.org/10.1117/1.JPE.15.024501

Efaz, E. T., Islam, M. S., & Islam, M. R. (2022). A review of simulation tools for thin-film solar cells. Materials, 15(21), 7832. https://doi.org/10.3390/ma15217832

Eltamaly, A. M., & Mohamed, M. A. (2021). Comparative study with practical validation of photovoltaic models. Scientific Reports, 11(1), 7348. https://doi.org/10.1038/s41598-021-84765-3

Green, M. A., et al. (2020). Solar cell efficiency tables (version 55). Progress in Photovoltaics: Research and Applications, 28(1), 3–15.

Hernández-Gutiérrez, C. A., Morales-Acevedo, A., Cardona, D., Contreras-Puente, G., & López-López, M. (2019). Analysis of the performance of $In_xGa_{1-x}N$ based solar cells. SN Applied Sciences, 1, 628, 1–10. https://doi.org/10.1007/s42452-019-0656-5

Hua, X. (2022). Parameters optimization of bilayer CIGS solar cell based on SCAPS-1D. Highlights in Science, Engineering and Technology (ESETEP), 5, 179–187.

Jackson, J., et al. (2016). High-efficiency CIGS thin-film solar cells with optimized bandgap and absorber thickness. Progress in Photovoltaics: Research and Applications, 24(7), 871–884.

Kasap, S. O. (2006). Springer Handbook of Electronic and Photonic Materials. Berlin: Springer.

Lu, S.-Y., Chien, C.-H., & Chen, C.-C. (2021). Analysis, modeling, and simulation of thin-film cells-based photovoltaic–thermoelectric generator hybrid system. Micromachines, 12(11), 1342. https://doi.org/10.3390/mi12111342

Mabvuer, F. T., Nya, F. T., Kenfack, G. M. D., & Laref, A. (2023). Lowering cost approach for CIGS-based solar cell through optimizing band gap profile and doping of stacked active layers—SCAPS modeling. ACS Omega, 8(3), 3256–3264. https://doi.org/10.1021/acsomega.2c06501

Mazur, T. M., Mazur, M., & Vakaliuk, I. (2023). Solar cells based on CdTe thin films (Part II). Physics and Chemistry of Solid State, 24(1), 134–145. https://doi.org/10.15330/pcss.24.1.134-145

Nakamura, K., Yamaguchi, Y., Kimoto, Y., Yasaki, T., Kato, H., & Sugimoto, M. (2019). Cd-free $Cu(In,Ga)(Se,S)_2$ thin-film solar cell with record efficiency of 23.35%. IEEE Journal of Photovoltaics, 9(6), 1863–1867. https://doi.org/10.1109/JPHOTOV.2019.2937218

Osman, Y., Fedawy, M., Abaza, M., & Aly, M. H. (2020). Solar cell performance enhancement with optimized CIGS absorber bandgap and buffer layer. Journal of Physics: Conference Series, 1447(1), 012057. https://doi.org/10.1088/1742-6596/1447/1/012057

Ramanujam, J., & Singh, U. P. (2017). Copper indium gallium selenide based solar cells—A review. Energy & Environmental Science, 10(6), 1306–1319. https://doi.org/10.1039/C7EE00573A

Rau, D., & Schock, H.-W. (2010). Electronic properties of CIGS heterojunctions and the role of interface defects. Applied Physics Letters, 97(18), 183502.

Saravanan, R., & Rajasekaran, K. (2022). A comparative study of different materials used for solar photovoltaic cell techniques. Materials Today: Proceedings. https://doi.org/10.1016/j.matpr.2022.04.421

Tyagi, V. V., Rahim, N. A., Selvaraj, J. A. L., & Kothari, R. (2013). Progress in solar PV technology: Research and achievement. Renewable and Sustainable Energy Reviews, 20, 443–461. https://doi.org/10.1016/j.rser.2012.09.028